JOURNAL OF GEOPHYSICAL RESEARCH, VOL. 111, C10018, doi:10.1029/2005JC003061, 2006

A quick response of the equatorial ocean to Antarctic sea ice/salinity anomalies

V. O. Ivchenko,[1] V. B. Zalesny,[2] M. R. Drinkwater,[3] and J. Schröter[4]

Received 17 May 2005; revised 27 February 2006; accepted 19 June 2006; published 31 October 2006.

[1] The potential mechanisms for a quick response of the equatorial ocean to processes occurring in the high-latitude Southern Ocean have been investigated. In the Southern Ocean at the Drake Passage latitudes, there is an zonally unbounded ''channel'', the Antarctic Circumpolar Current Belt (ACCB). It is demonstrated that in a multiconnected domain such as the ACCB, signals generated by anomalies in the Southern Ocean sea ice cover/salinity distribution can propagate in a wave-like manner in the form of fast moving barotropic Rossby waves. A disturbance induced near the Drake Passage is demonstrated to generate a Rossby wave that propagates across the Pacific in only a few days. This signal is reflected at the western boundary of the Pacific and generates an equatorward propagating coastally trapped Kelvin wave. The resulting temperature anomaly moves northward along the western coastline up to the vicinity of the equator and increases in amplitude over time. The anomaly in the western edge of equatorial Pacific then begins to propagate eastward along the equator as a trapped equatorial wave. After about 2–3 months this wave reaches the eastern coast, reflects, and generates the coastal trapped wave, which propagates north and south along the coastline in both hemispheres. This process is suggested as one possible direct mechanism by which the extratropical ocean can induce anomalies in the equatorial ocean.

Citation: Ivchenko, V. O., V. B. Zalesny, M. R. Drinkwater, and J. Schröter (2006), A quick response of the equatorial ocean to Antarctic sea ice/salinity anomalies, *J. Geophys. Res.*, *111*, C10018, doi:10.1029/2005JC003061.

1. Introduction

[2] Various analyses have revealed links in the form of statistically significant correlations or ''teleconnections'' between Antarctic sea ice anomalies and global climate variability [*Carleton*, 1988; *Simmonds and Jacka*, 1995; *Bromwich et al.*, 1998; *Yuan and Martinson*, 2000; *Kwok and Comiso*, 2002]. *Carleton* [1988] finds a signal of the Southern Oscillation in the data from the summer ice conditions in the northern Weddell sea, for the period of time between 1929 and 1962. *Bromwich et al.* [1998] studied atmospheric impacts induced by year-round open water adjacent to Antarctica. As a result of sea ice removal, the authors have shown substantial changes in pressure, precipitation and vertical circulation in both hemispheres. *Simmonds and Jacka* [1995] investigated links between Antarctic sea ice extent and the Southern Oscillation index (SOI) by using 20 years of data (1973–1992). Their results support the suggestion that there are key regions that influence and are influenced by the Southern Oscillation. They found that not only can the SOI lead sea ice extent, but that sea ice extent also can lead to SOI. *Yuan and Martinson* [2000] and *Kwok and Comiso* [2002] identify several similar, compelling teleconnection patterns that implicate a link between sea ice variability and tropical ocean and atmosphere variability. One of these is between the western central tropical Pacific and the eastern south Pacific region of the Antarctic. In the Amundsen, Bellingshausen and Weddell sectors of the Southern Ocean, for instance, *Kwok and Comiso* [2002] found the strongest correlation between the Southern Oscillation and sea ice anomalies, with a lag that is dependent on longitude. One of the reasons proposed for the interannual and interdecadal variation in the Southern Ocean could be El Nino–Southern Oscillation (ENSO) signals propagating to high latitudes [*White and Peterson*, 1996]. The correlation between anomalies in Antarctic sea ice extent and standard indices of ENSO imply that 40% of the variance in the sea ice anomalies is attributable to ENSO [*Yuan et al.*, 1996].

[3] Some studies attribute the connection between low and middle latitudes and polar regions to atmospheric processes involving long-wavelength, propagating [*James*, 1988], or quasi-stationary Rossby waves [*Karoly*, 1989]. *Meredith et al.* [2004] present the first direct evidence that variability in the Southern Annular Mode (SAM) forces interannual variability of the ocean transport through the Drake Passage (SAM is the strongest mode of climate variability in the Southern Hemisphere outside the tropics). It is important to note that this result is based both on the

[1]National Oceanography Centre Southampton, Southampton, UK.
[2]Institute of Numerical Mathematics, Russian Academy of Sciences, Moscow, Russia.
[3]European Space Research and Technology Centre, European Space Agency, Noordwijk, Netherlands.
[4]Alfred Wegener Institute for Polar and Marine Research, Bremerhaven, Germany.

0148-0227/06/2005JC003061$09.00

observations of the western Antarctic Peninsula, and on experiments with an ocean model. *Mo and White* [1985] find the teleconnections patterns in the Southern Hemisphere (SH). It was demonstrated that teleconnectivity in sea level pressure in summer is dominated by the Southern Oscillation. They found a weak ''see-saw'' between Australia and the Southern Ocean south of Australia. There are a number of papers on teleconnection in the SH. A broad modern physical interpretation, as well as a list of publications can be found in the review of the atmospheric teleconnections by *Turner* [2004].

[4] Note, that until recently none explicitly invoke ice-ocean-related processes. *Peterson and White* [1998] were the first to mention an oceanic and sea ice interconnection with a 4 year periodicity, but sea ice responds passively to atmospheric forcing. *Venegas et al.* [2001] further investigated the spatial patterns in sea ice extent, drift and sea level pressure associated with such quasi-quadrennial, coupled anomalies. They suggest that freshwater anomalies (and stratification) resulting from a combination of anomalous meridional ice drift (i.e., freshwater flux) and ice edge melting could potentially be responsible for persistence of anomalous ocean-atmosphere heat fluxes that feedback into the atmospheric conditions. *Venegas and Drinkwater* [2001] implicate such processes in explaining the linked quasi-quadrennial coupled anomalies in the Weddell Sea. They suggest that the strong teleconnection between ENSO and atmospheric forcing conditions in this region results in the generation of periodic sea ice thickness anomalies that are transported in the Weddell gyre. These anomalies have persistence times which are governed by the drift rate and the time the ice survives in the circulation before being carried northward into warmer water and melting.

[5] The mean clockwise gyre circulation in the Weddell Sea carries ice equatorward in the region east of the tip of the Antarctic peninsula. Export of sea ice into the Antarctic Circumpolar Belt occurs in a zone between approximately $-55°$ and $-35°$W where the sea ice melts as it encounters warmer surface waters. At typical mean drift speeds of 3 km d^{-1} the monthly mean export computed over an interval of six years is 32×10^3 m^3 s^{-1} [*Drinkwater et al.*, 2001], equivalent to a mean freshwater transport of 0.032 Sv. Month to month, and seasonal to interannual variations are observed in sea ice transport, with periodic anomalies superimposed on the mean seasonal cycle. The appearance and subsequent advection of periodic sea ice thickness anomalies is substantiated by satellite and Upward Looking Sonar sea ice thickness observations in the Weddell Sea [*Strass and Fahrbach*, 1998; *Drinkwater et al.*, 2001]. Observations indicate that anomalies appearing in summer season sea ice concentrations and meridional winds of *Venegas and Drinkwater* [2001] are strongly related to the formation of coastal ice growth and thickness anomalies. Circulation of resulting ice thickness anomalies within the Weddell gyre can cause significant month-to-month and year-to-year variability in freshwater export from the Weddell Sea [*Drinkwater et al.*, 2001; *Harms et al.*, 2001]. These results indicate that month-to-month, wind-driven variability superimposed on ENSO-related interannual oscillations can lead to extreme monthly sea ice export (volume flux) anomalies of the order of $100 \times 10^3 m^3 s^{-1}$ (or 0.1 Sv), as occurred under rapid wind drift conditions in winter 1992. Such ice export anomalies can exceed three times the monthly mean, and are equivalent to approximately 1 m/month ice melt over an area of 500,000 km^2, at around 60°S: they are thus of equivalent order of magnitude to the typical net annual melt rate of 1 m/year in this location [*Timmermann et al.*, 2001]. The freshwater anomaly area corresponds to the predominant outflow region of the Weddell gyre, where sea ice encounters the warm waters of the Antarctic Circumpolar Current (ACC). *Zhang and Semtner* [2001] reproduced winter 1992 salinity and temperature anomalies of -0.1 psu and $-0.5°$C, respectively [*Zhang and Semtner*, 2001, Figure 1] in the upper ocean at 56°S in this ice export region of the Weddell Sea, as a consequence of freshwater export anomalies.

[6] There are two different climate relevant forms of ocean processes responsible for anomaly propagation or signal transport in the ocean component of the climate system. One is based on advection in the thermohaline circulation, and has characteristic timescales of hundreds to thousands of years. Another rather quicker process is based on wave-like propagation of the signal and has characteristically shorter timescales of days to months. In this paper, we restrict discussion to wave propagation, whereby if sea surface temperature (SST) is affected by such a signal it could act to modify the atmosphere/ocean interaction. If this interaction is strong, it could lead to important consequences for the climate system in timescales of months to years.

[7] The global atmosphere is especially sensitive to SST fluctuations in the tropics because of the deep convective atmospheric boundary layer there. Small SST gradients fluctuations can lead to shifts in the location of large-scale convection and result in large anomalies in atmospheric heating [*Trenberth et al.*, 1998]. To date, we are aware of only a few studies in which ocean communication between the extratropics and tropics is studied in detail. *Peng and Wang* [1989] used a model to suggest that atmospherically induced strengthening and progressive northward movement of cold ocean currents can impact the large-scale atmospheric circulation. *Bromwich et al.* [1998], however, find that the signal of equatorward propagation of the polar signal occurs along the western Pacific, contrary to Peng and Wang's model results.

[8] In this paper we investigate the possibility of the equatorial response to anomalies in the Southern Ocean. The focus is on wave-like propagation of anomalies initiated by freshwater/salinity anomalies in the location of the Antarctic peninsula, the consequences of which provide a response more consistent with the observations of *Bromwich et al.* [1998]. The mechanism investigated also provides a more rapid communication mechanism between extratropical and tropical oceans than those ocean processes previously investigated. In the recent studies a rapid propagation of the signal introduced by the salinity anomaly in the Antarctic to the equatorial ocean was demonstrated by employing models of the ocean [*Ivchenko et al.*, 2004] and the coupled ocean/atmosphere model [*Richardson et al.*, 2005]. However, these papers did not evaluate such important factors as the influence of bottom topography on the propagating signal. They also do not reveal how the salinity anomaly results in a source of barotropic Rossby waves in the source area, and the direction of propagation of Rossby and Kelvin waves.

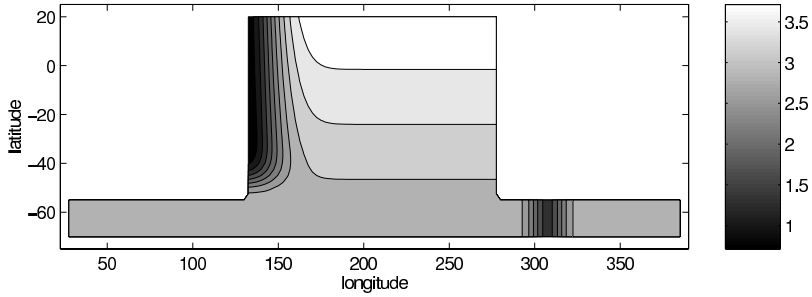

Figure 1. The INM model domain. The bottom relief for the Experiment STANDARD is indicated: units are in kilometers, contour interval is 0.3 km, and the contours range from a minimum of 0.3 km to a maximum depth exceeding 3.5 km.

[9] *Kawase* [1987] studied the initiation and propagation of a Kelvin wave along the coast and the equator by using a linear two-layer model, representing thermocline and deep layers. The coastal Kelvin wave propagates from the northwest corner equatorward along the western boundary. Upon reaching the equator it excites an equatorial Kelvin wave, which travels eastward along the equator. After reaching the eastern boundary the Kelvin wave separates and travels poleward in both hemispheres, and also radiates a long Rossby wave. As the greatest group velocity of the long Rossby wave is achieved on the equator, and decreases poleward, the equatorial region is first affected. The velocity field is established after about 200 days.

[10] Particular aims of this study are as follows: (1) can sea ice/salinity anomalies initiate similar wave-like propagation in the ocean from a particular part of the Southern Ocean to the equatorial regions, and (2) what kind of wave participates and how quick is the equatorial response?

[11] Employing the general circulation model with real bottom topography leads to complications in understanding the physical mechanisms responsible for propagation of the signal from the Antarctic to the equator. We think that such a study should be started by applying a model with a simplified geometry, like a zonal channel (to simulate the ACC Belt) with a rectangular basin to the north (to simulate the Pacific Ocean). The model we employed was the σ coordinate INM model (the model of the Institute of Numerical Mathematics, Moscow) [*Zalesny*, 1996] (see Appendix A).

[12] In this study we investigate the mechanisms of a rapid propagation of the surface anomaly from the ACCB area to the equatorial ocean. The absolute values of the initial perturbing anomaly and life time used here are artificial. The initial anomaly was prescribed as instantaneous, which is a common approach in climate research. It is not our goal at this stage to reveal the climate significance of such propagation, rather the main aim of our manuscript is to investigate how quickly the initial disturbance in the ACCB can propagate to the equatorial ocean along with the responsible physical mechanism. An additional aim is to demonstrate how the change in relative amplitudes of the initial disturbances and their duration influences the equatorial response. The other important problems studied in the paper are the influence of topography on the propagation of the signal, the energy conversion in the system (how the anomaly of salinity generates a barotropic Rossby wave) and direction of signal propagation.

2. Numerical Experiments With the INM Model

2.1. Model Domain and Parameters

[13] The INM model domain is an area consisting of two connected parts: a zonal periodic channel and a rectangular basin, representing the Southern Ocean and Pacific respectively (Figure 1). We restrict the northern boundary of the Pacific domain at 20°N latitude, to concentrate our study on the dynamics of the Southern Ocean and equatorial Pacific.

[14] The wind stress was derived from 1990–1995 time averaged ECMWF wind, by taking zonal average over the Pacific. Then a polynomial approximation to that field was used (see Appendix A). The profiles of wind stress, surface temperature and salinity can be seen on Figure 2.

[15] The ocean domain is approximated on two grids. A standard grid $2.5^\circ \times 2.5^\circ \times 12$ (2.5 degrees latitude and longitude, and 12 σ levels) and a second grid with higher meridional resolution of $2.5^\circ \times 0.83^\circ \times 12$ were used.

[16] The turbulent coefficients (see Appendix A) were:

$$\nu_u = \nu_v \equiv 2 \quad cm^2/s, \quad (\nu_T)_{\min} = (\nu_S)_{\min} \equiv 1 \quad cm^2/s,$$

$\mu_u = \mu_v = \mu_T = \mu_S \equiv 2 \cdot 10^7$ cm^2/s and restoring coefficient $\alpha = 0.04$ cm/s. The model time step was equal to 12 hours, for horizontal resolution $2.5^\circ \times 2.5^\circ$, and 4 hours for resolution $2.5^\circ \times 0.83^\circ$. The choice of comparatively high turbulent and restoring coefficients was to decrease computer time for numerical runs.

[17] Numerical experiments were conducted in two stages. In the first stage the equilibrium solution is calculated starting from the following initial conditions:

$$u = 0, \qquad v = 0, \qquad T \equiv const = 4^\circ C, \qquad S \equiv const = 34\, psu.$$

[18] During the second stage (anomaly runs), a local sea surface salinity (SSS) anomaly is applied at the sea surface in the vicinity of the ACC bathymetric obstacle (Figure 1) at 60°S, 300°E. All these experiments were started from an equilibrium solution obtained at the first stage and carried out over a two to ten year simulation period.

2.2. Equilibrium Regimes

[19] The first aim in our experiments is to find the model equilibrium solution. For stationary forcing, the system

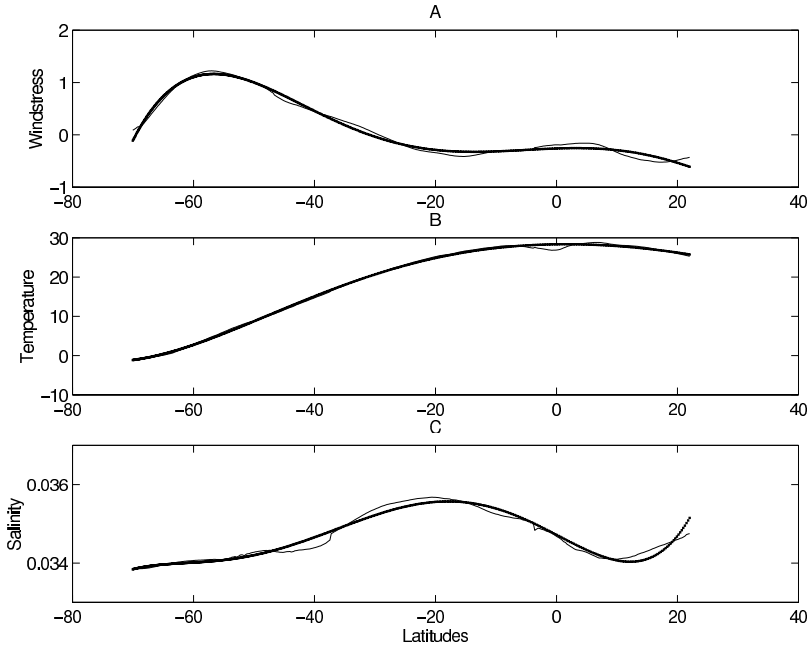

Figure 2. (a) The zonally averaged kinematic wind stress magnitude, from time-averaged ECMWF wind velocity over the Pacific (the thin line). The thick line represents the polynomial approximation. The units are in $cm^2 s^{-2}$. (b) The zonally averaged surface temperature is from *Levitus* [1982] Pacific data (the thin line). The thick line represents the polynomial approximation. The units are in °C. (c) The zonally averaged surface salinity is from *Levitus* [1982] Pacific data (the thin line). The thick line represents the polynomial approximation. The units are in psu/1000.

must reach equilibrium or find a quasi-stationary regime of oscillation. Using similar forcing and initial conditions, the difference between such equilibrium regimes depends on bottom topography. So, we have calculated four equilibrium states for four different topographies (see section 3).

[20] Bottom topography, in numerical experiments with simplified geometry domain, should be also idealized. However, such idealization should be either physically reasonable or provide the simplest type. So, one of the experiments is with the simplest topography: a flat bottom. Another experiment is worthwhile with large-scale meridional slope in the Pacific, since the zonally averaged bottom topography in the Pacific increases from the Northern to the Southern Pacific by about 1 km. We propose that barotropic Rossby waves play an important role in the propagation of the signal from the ACCB to the western Pacific. Their generation by thermohaline forcing is possible only under variable topography, and therefore we introduce in all experiments the ACC Gaussian bump at the model longitude of about 300°, which represents the Scotia Island Arc, the height of which is 1.5 km (Figure 1). We also suppose that the Kelvin waves along the western Pacific are important for anomaly propagation along the western coast. Thus, in some experiments we constructed a slope/shelf along the western coastline of the Pacific of about 20° east–west extent, and the depth varies by about 800 m between the Western and the Eastern boundaries of the shelf.

[21] We use the following types of bottom topography (BT):

[22] 1. Bottom topography comprises flat bottom topography in the ACCB (depth of 3 km) everywhere except the ACC bump. There is the western Pacific slope/shelf (see Figure 1). In the rest of the Pacific the depth has a large-scale meridional slope of 1 km from the north to the south.

[23] 2. The same as BT1, but the western Pacific slope/shelf is removed.

[24] 3. The same as BT1, but the Pacific topography is constant everywhere and equal to the ACC depth (3 km).

[25] 4. The same as BT1, but the meridional ridge was introduced as a latitudinally stretched mountain with the height of 1.5 km (see Figure 3), simulating the East Pacific Rise.

[26] Model spin up achieved equilibrium after about 2000 years of integration for all model configurations. In all these equilibria the kinetic energy, potential energy and the ACC transport are almost constant after 2000 years.

[27] Comparing the equilibrium solution with climatology [*Stephens et al.*, 2002] and the WOCE Atlas for the Southern Ocean [*Orsi and Whitworth*, 2005] show that the idealized model reproduced the climatology (temperature and salinity distribution, as well as large-scale circulation) qualitatively well. However, the difference in values could be large. For example the ACC transport in all experiments is between 40 and 60 Sv, which is much smaller than the observed values of about 130–150 Sv in the Drake Passage [*Cunningham et al.*, 2003; *Grezio et al.*, 2005]. Such a big difference results from the exclusion of the Atlantic and Indian Oceans, and simplified geometry. All these factors substantially influence the meridional overturning in the Southern Ocean and consequently affect the ACC transport [*Ivchenko et al.*, 1996; *Olbers and Ivchenko*, 2001]. In the section along 60°S temperature variation is in reasonable agreement with the observations. At 50 m depth the averaged equilibrium tempera-

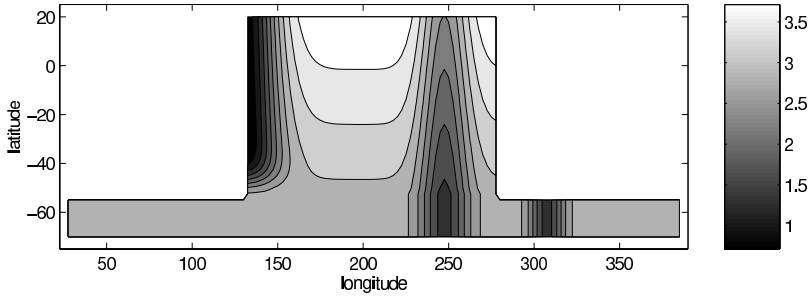

Figure 3. The INM model domain. The bottom relief for the Experiment RIDGE is indicated: units are in kilometers, contour interval is 0.3 km, and the contours range from a minimum of 0.3 km to a maximum depth exceeding 3.5 km.

ture is 2.5°C vs 3.0°C in observations (variation along 60°S in the Pacific is between 0.0° and 5.0°C). At the depth of 2500 m the equilibrium averaged temperature is about 1.0°C vs 0.93°C from observations (variations are between 0.2° and 1.3°C). In the upper Southern Ocean salinity is in reasonable agreement with observations, but becomes worse away from the surface: the equilibrium vertical distribution is too homogeneous.

[28] In the equatorial region the range of the variation of temperature of modelled equilibrium and climatology are reasonably similar: between 28.0° (equilibrium) and 29.0°C (climatology) (at the surface in the West Pacific) and 3.0° (equilibrium) and 2.0° (climatology) at a depth of 2500 m. The western/eastern asymmetry in the upper equatorial ocean is more pronounced in the climatology compared to numerical equilibrium. We suppose that general temperature/salinity structure of the equilibrium of the idealized model is good enough for our purpose of studying propagation of the signal.

2.3. Main Outlook of Obtained Results

[29] Nine individual numerical experiments have been carried out with different bottom topography, space resolution, position, amplitude and duration of initial sea surface salinity (SSS) anomaly (see Table 1).

[30] The primary response, common to all experiments, is the excitation of an SST anomaly along the western Pacific boundary, and generation of an eastward propagating equatorial Kelvin wave, which reaches the east coast and excites a temperature anomaly that travels poleward as a trapped coastal Kelvin wave. The most intriguing thing is how quickly the signal propagates from the source to the western Pacific: over this very long path of about 10,000 km, the signal arrives in just about a few days. This signal is weak, but greatly increases over time. In the stream function structure it results in boundary modes with surging amplitudes (Figure 4). The propagation of the signal occurs by barotropic Rossby waves, generated in the vicinity of the ACC bump, which have a very high speed. Taking into account that the ocean depth in the area of the ACCB is constant, we can estimate longitudinal group velocity c_x:

$$c_x = -\frac{\beta\left(k_y^2 - k_x^2\right)}{|\ k\ |^4} \tag{1}$$

where $|k|^2 = k_x^2 + k_y^2$, $\beta = \frac{\partial l}{\partial y}$, l is Coriolis parameter, k_x, k_y are longitudinal (x) and latitudinal (y) wave numbers. The highest longitudinal group velocity is about of 40 m/s^{-1} for $\beta = 2 \cdot 10^{-11}$ $m^{-1}s^{-1}$, $k_y \approx 7 \cdot 10^{-7}$ m^{-1} and $k_y^2 \gg k_x^2$.

[31] At this group velocity it would take around 3 days to cross the 10^4 km distance between the ACC bump and western Pacific: this is in good agreement with our results. Note, the above estimation is only valid under conditions of an unbounded ocean, which is a reasonable approach for the ACC. However, after arrival of the barotropic signal to the western boundary, a nonstationary boundary layer starts to form. That results in formation of a baroclinic signal and propagation of the boundary Kelvin waves toward the equator. The timescale T of formation of such a nonstationary boundary layer with the width of L_h can be estimated from $T \sim \frac{1.4}{\beta \cdot L_h}$ following *Lighthill*'s [1969] theory. Supposing L_h is equal to the half of longitudinal mesh size, T is approximately 8 days. It is in a reasonable agreement with the formation of the barotropic boundary layer near the southern Pacific western coast (see Figure 4).

[32] An experiment was conducted with Rossby waves being switched off, to study the possible mechanism for anomaly propagation. For that purpose we retained an "undisturbed" barotropic stream function field during the

Table 1. Parameters of the Experiments

Experiment	Magnitude and Duration of Initial Anomaly	Resolution	Position of Anomaly	Topography
STANDARD	2 psu/60 days	2.5°	western side (WS) of bump	BT1
HIGH-RES	2 psu/60 days	2.5° (in longitude) 0.83° (in latitude)	WS	BT1
NO-SHELF	2 psu/60 days	2.5°	WS	BT2
FLAT	2 psu/60 days	2.5°	WS	BT3
STANDARD-E	2 psu/60 days	2.5°	eastern side (ES) of bump	BT1
STANDARD-ONE	1 psu/120 days	2.5°	WS	BT1
STANDARD-HALF	0.5 psu/240 days	2.5°	WS	BT1
STANDARD-QUARTER	0.25 psu/360 days	2.5°	WS	BT1
RIDGE	2 psu/60 days	2.5°	WS	BT4

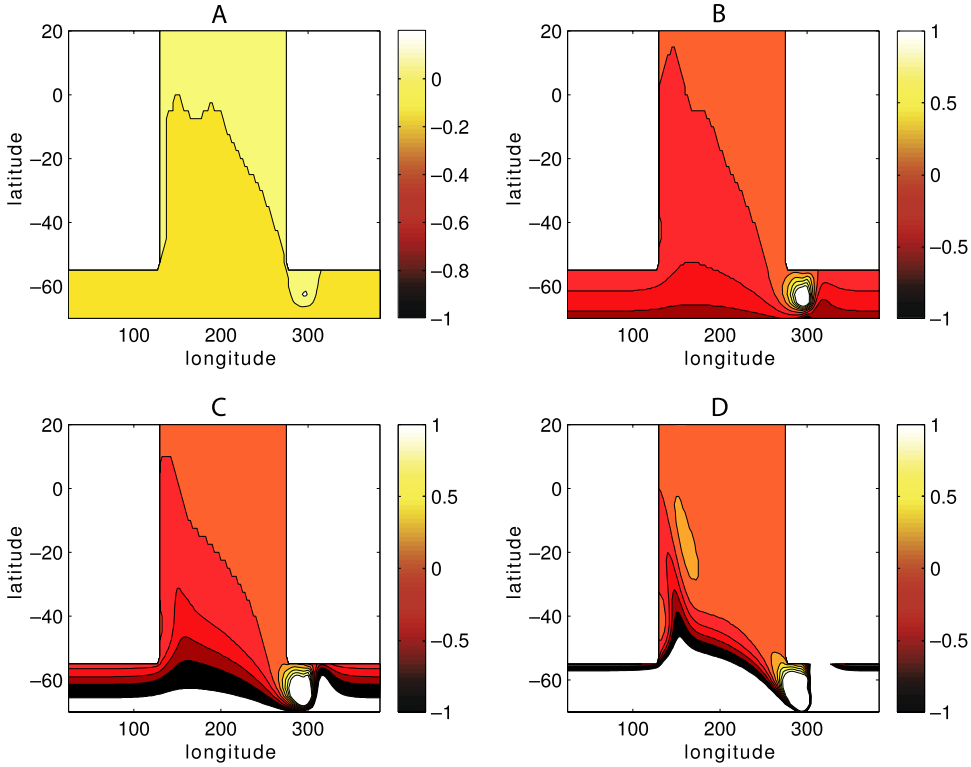

Figure 4. Stream function anomaly for four consecutive times: (a) 1, (b) 3, (c) 5, and (d) 10 days in Exp.STANDARD. The units are in sverdrups (10^{12}cm^{3}s^{-1}).

experiment with perturbation. We found that in this case the western boundary modes are not generated, and the temperature field remains undisturbed.

[33] In all experiments there is a rapid formation of the temperature anomaly along almost the whole western boundary layer from the southwestern corner of Pacific to the equator (Figures 5–7). The magnitude of the anomaly develops over time equatorward in a wave-like manner. This process includes an interaction of basin-scale barotropic and Kelvin-like boundary modes. The Kelvin-like boundary mode results as an interaction between barotropic (depth averaged) motion. The structure of this feature depends on the model space resolution. Coarse resolution, which does not correctly resolve the baroclinic Rossby-scale processes, could distort such a structure. However, this distortion is moderate even for coarse resolution, and resultant propagation speeds are, in spite of this effect, close to fine resolution speed [*Johnson and Marshall*, 2002].

[34] The sensitivity experiments (Table 1) show that the sign of the temperature anomalies changes between the different runs (Exp.STANDARD and Exp.HIGH-RES, Figures 8–9; and Exp.NO-SHELF, Exp.FLAT and Exp.STANDARD-E, Figures 10–11) and with time for the given experiment (Exp.STANDARD, Figure 8; Exp.HIGH-RES, Figure 9; and Exp.STANDARD-E, Figure 11). Two important questions arise from our experiments: what is the main reason for the generation of disturbances at the western Pacific shelf, and by what means are these disturbances transported along the equatorial Pacific belt from the western to the eastern coast?

[35] All experiments show that in equilibrium the upper layer on the western part of the equatorial and tropical Pacific has weak or neutral stratification, which coincides with climatology [*Stephens et al.*, 2002]. Both the incoming barotropic signal and the generated baroclinic signal can strongly affect weakly stable ocean columns in the western equatorial/tropical Pacific in the upper 300 meters and cause mixing in the upper 1–4 layers, and as a result the temperature anomaly is rather strong in that area. Momentum and potential density fields lose their dynamical consistency causing propagation of corresponding temperature disturbances along the equatorial belt.

[36] One can see variability in temperature anomaly propagation (Figures 5–9). The time-space characteristics of anomaly propagation along the equator resulted from the modal structure of the equilibrium state, and depends on undisturbed potential density stratification. To estimate these values, particularly the speed of propagation of the temperature anomaly, one can apply traditional analysis assuming a linear character for equatorial dynamics at the restricted time interval around several weeks [*Philander and Pacanowski*, 1980; *Delecluse and Zalesny*, 1996]. The velocity of the propagation of the baroclinic mode number n (C_n) is inversely proportional to the square root of eigenvalue λ_n [*Delecluse and Zalesny*, 1996]:

$$C_n^2 = H/\lambda_n \tag{2}$$

where H is the depth of the ocean.

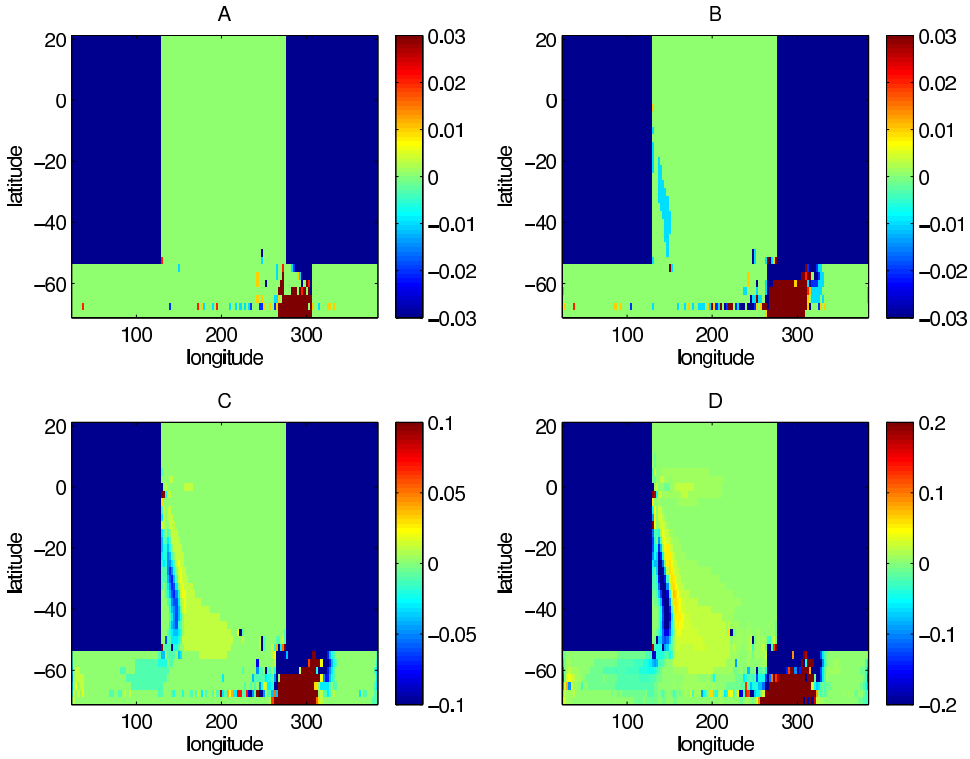

Figure 5. The subsurface temperature anomaly (at the second layer) at four consecutive times (t = (a) 1, (b) 15, (c) 31, and (d) 47 days) in Experiment STANDARD. The units are in °C.

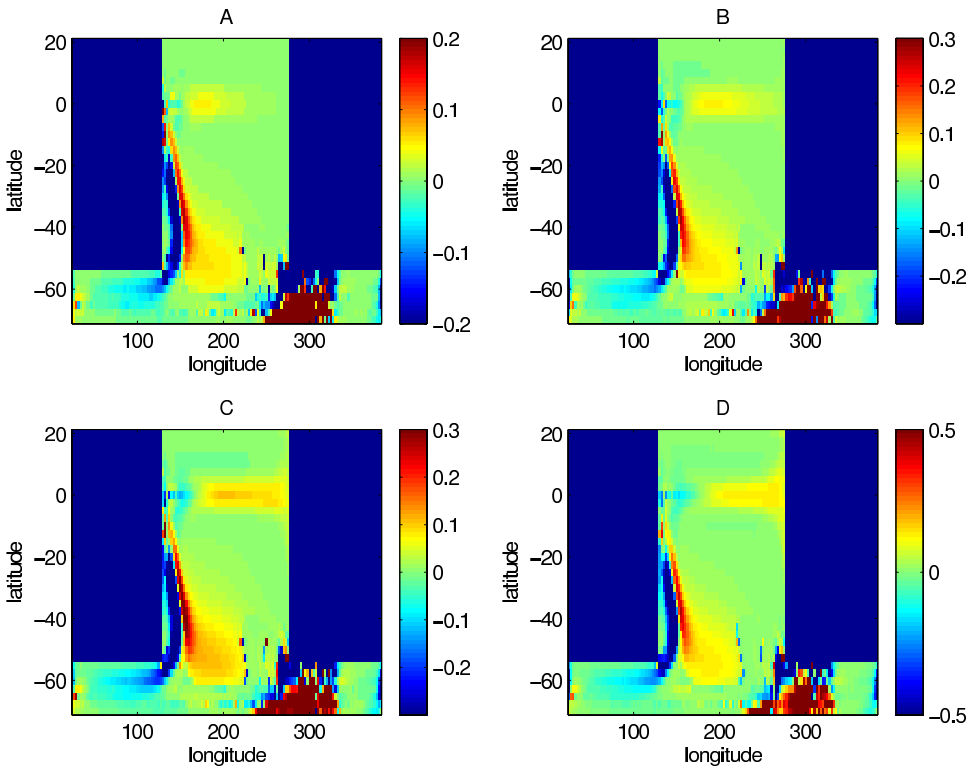

Figure 6. The subsurface temperature anomaly (at the second layer) at four consecutive times (t = (a) 63, (b) 79, (c) 95, and (d) 111 days) in Experiment STANDARD. The units are in °C.

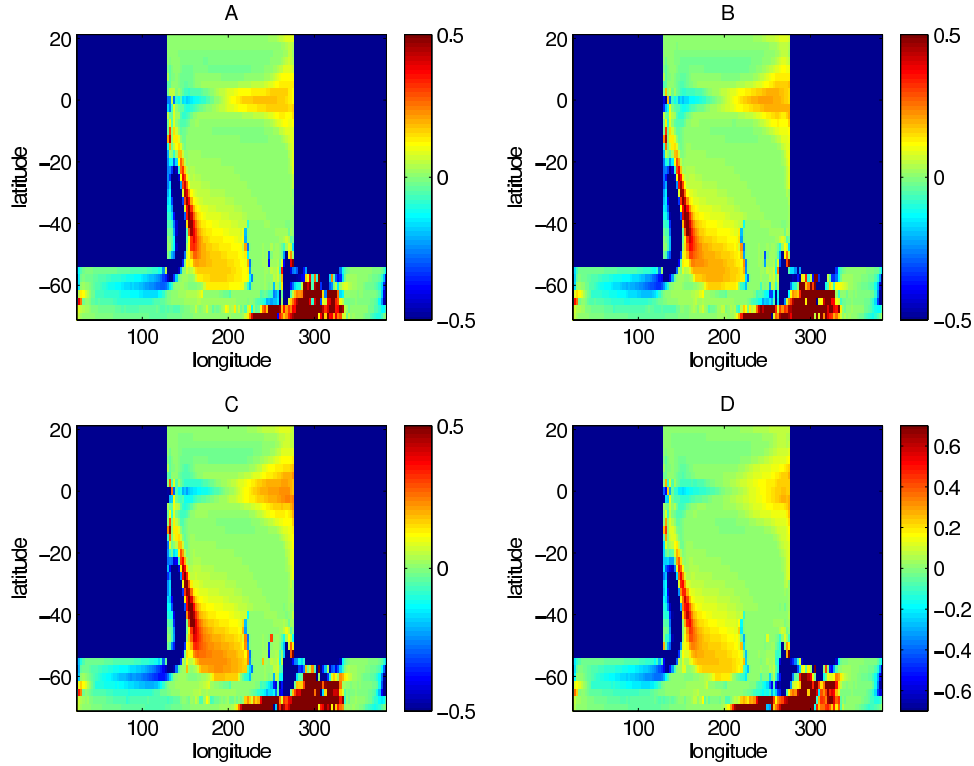

Figure 7. The subsurface temperature anomaly (at the second layer) at four consecutive times (t = (a) 127, (b) 143, (c) 159, and (d) 175 days) in Experiment STANDARD. The units are in °C.

[37] In case of Exp.STANDARD one can estimate $\lambda_1 = 3.46 \cdot 10^2\ s^2m^{-1}$, $\lambda_2 = 12.3 \cdot 10^2\ s^2m^{-1}$, $C_1 = 2.94\ ms^{-1}$, $C_2 = 1.56\ ms^{-1}$. The time propagation of the corresponding modes along equatorial basin is $T_1 = 59$ days, $T_2 = 111$ days. The time taken for the first mode to propagate from the western Pacific to the Eq2, Eq3, and Eq4 is approximately 20, 40, and 60 days, respectively, which is in good agreement with Exp.STANDARD. The second baroclinic

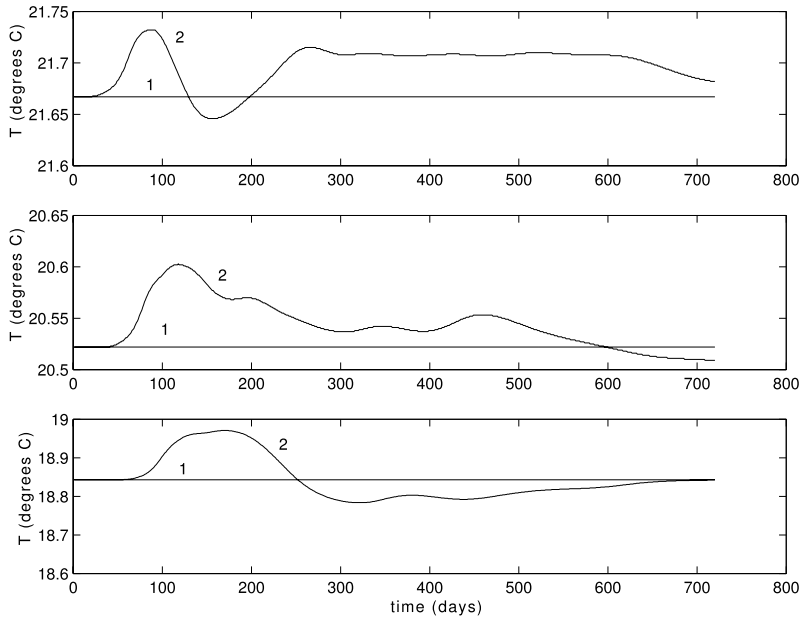

Figure 8. The mean temperature at the second layer in subdomains (top) Eq2, (middle) Eq3, and (bottom) Eq4. An almost constant value line (1) in each region represents the equilibrium Exp.STANDARD. Another line (2) represents the anomaly experiment STANDARD. All the subdomains are the 10° boxes, and their centers are positioned in the equator of the Pacific: Eq2 in the longitude of 177.5°E, Eq3 in the longitude of 225°E, and Eq4 in the longitude of 267.5°E. The units are in °C.

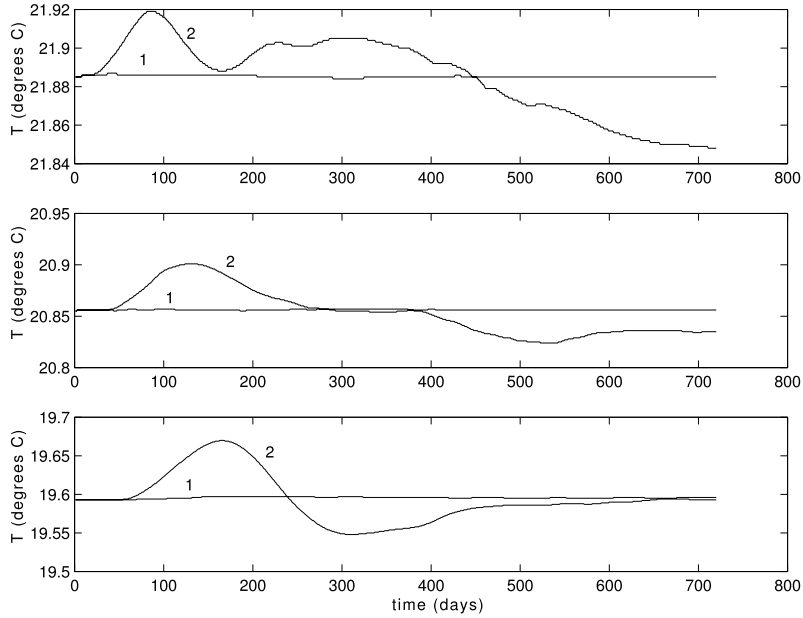

Figure 9. The mean temperature at the second layer in subdomains (top) Eq2, (middle) Eq3, and (bottom) Eq4. An almost constant value line (1) represents the equilibrium Exp.HIGH-RES. Varying lines (2) represent the anomaly experiment Exp.HIGH-RES. Positions of subdomains Eq2, Eq3, and Eq4 are the same, as in Figure 8. The units are in °C.

mode propagates 1.9 times more slowly than the first. In Figure 7 (the subsurface temperature anomaly after 127, 143, 159, and 175 days) one can see that after a positive anomaly, a negative anomaly follows, propagating eastward from the western Pacific along the equator.

[38] Looking at the pictures representing time series of the mean temperatures in subdomains Eq1–Eq4 for the all additional numerical experiments, one can also see that the first incoming signal (to the eastern equatorial

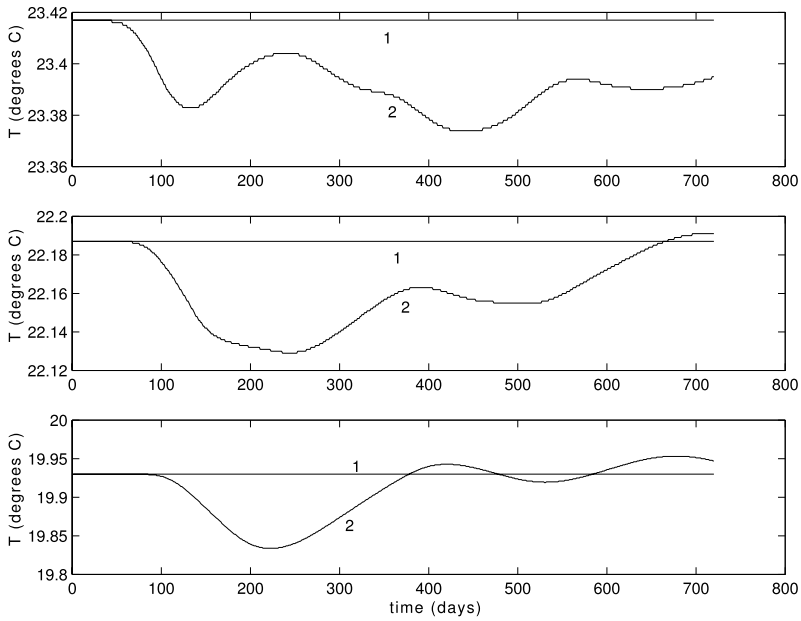

Figure 10. The mean temperature at the second layer in subdomains (top) Eq2, (middle) Eq3, and (bottom) Eq4. An almost constant value line (1) represents the equilibrium Exp.FLAT. Varying lines (2) represent the anomaly Exp.FLAT. Positions of subdomains Eq2, Eq3, and Eq4 are the same, as in Figure 8. The units are in °C.

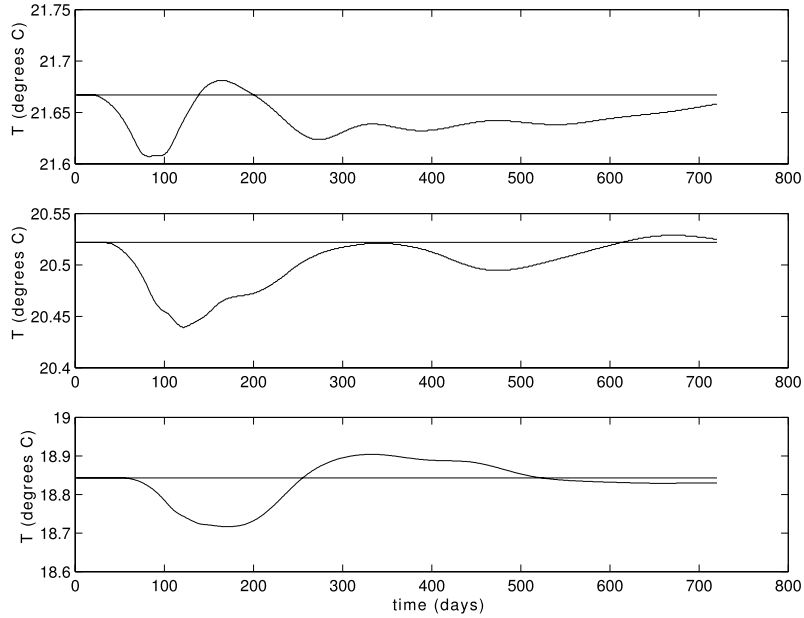

Figure 11. The mean temperature at the second layer in subdomains (top) Eq2, (middle) Eq3, and (bottom) Eq4. An almost constant value line represents the equilibrium Exp.STANDARD-E. Varying lines represent the anomaly Exp.STANDARD-E. Positions of subdomains Eq2, Eq3, and Eq4 are the same, as in Figure 8. The units are in °C.

Pacific) is propagated by means of the first baroclinic mode.

3. Results of Experiments

[39] All experiments have been started with the same initial conditions (see section 2.1), with the same model parameters and first achieved equilibrium over 2000 years. After that the SSS anomaly was placed over the topography feature. Then the experiments were carried out over a two to ten years simulation period.

3.1. Experiment STANDARD

[40] The anomaly run demonstrates a rapid response to the 2 psu SSS anomaly with a signal reaching the western Pacific within a few days (Figure 4).

[41] The stream function anomaly in the Southern Ocean domain propagates westward very quickly around the ACC: after 1.5–2 days the anomaly reaches values of about −1 to +1 Sv everywhere (Figure 4). Subsequently the anomaly propagates to the Pacific domain, with a substantial northwest wave velocity component.

[42] The signal travels to the western boundary of the Pacific and generates a temperature anomaly along the western coastline up to the vicinity of equator (Figure 5). The amplitude of the temperature anomaly increases over time, and after several days it reaches an averaged value of order 0.05°–0.1° in particular 10° subregions. The local (without any averaging) temperature anomaly extrema near the western Pacific is an order of magnitude greater (see sections 3.7 and 4).

[43] The anomaly in the western boundary of the equatorial Pacific starts to propagate eastward along the equator as a trapped equatorial Kelvin wave (Figure 5). After about 2–3 months this wave reaches the eastern coast, reflects, and generates the coastal trapped wave, which travels along the coastline in both hemispheres (Figure 5). The magnitude of the temperature anomaly increases and reaches values of more than 0.1° at the eastern equatorial Pacific 120 days after the start (Figure 8).

[44] In Figure 8 one can see the evolution of the temperature, averaged over the two upper layers in several model subdomains. The signal propagates from west to the east, along the equator. It is visible in subdomains Eq2, Eq3, and Eq4 after about 20, 40, and 60 days, respectively. The amplitude increases eastward from 0.06° at Eq2 after 90 days to 0.08° at Eq3 after 118 days, and to 0.13° at Eq4 after 177 days.

[45] The total kinetic energy of the whole basin reaches the highest value after 50 days before steadily falling. Equilibrium is restored after about 10 years of integration.

3.2. Experiment HIGH-RES (Increased Resolution)

[46] The main structure of the stream function in this experiment (Figure 12) looks similar to the Exp.STANDARD. However, the ACC transport decreases from 53.3 Sv (Figure 12a) in Exp.STANDARD to 47.6 Sv in Figure 12b. At the same time the Pacific gyre is strongly intensified, from −41.5 to −59.1 Sv. A profound interaction takes place between the gyre and the ACC; the gyre penetrates into the ACC area, and the isolines of the stream function of the ACC are shifted to the south in the Pacific sector of the Southern Ocean.

[47] The anomaly run of Exp.HIGH-RES nonetheless also demonstrates a quick response in the temperature field. The time of propagation of the temperature anomaly along equator is nearly the same as in Exp.STANDARD (Figure 9). The horizontal turbulent coefficients μ_u, μ_v, μ_T

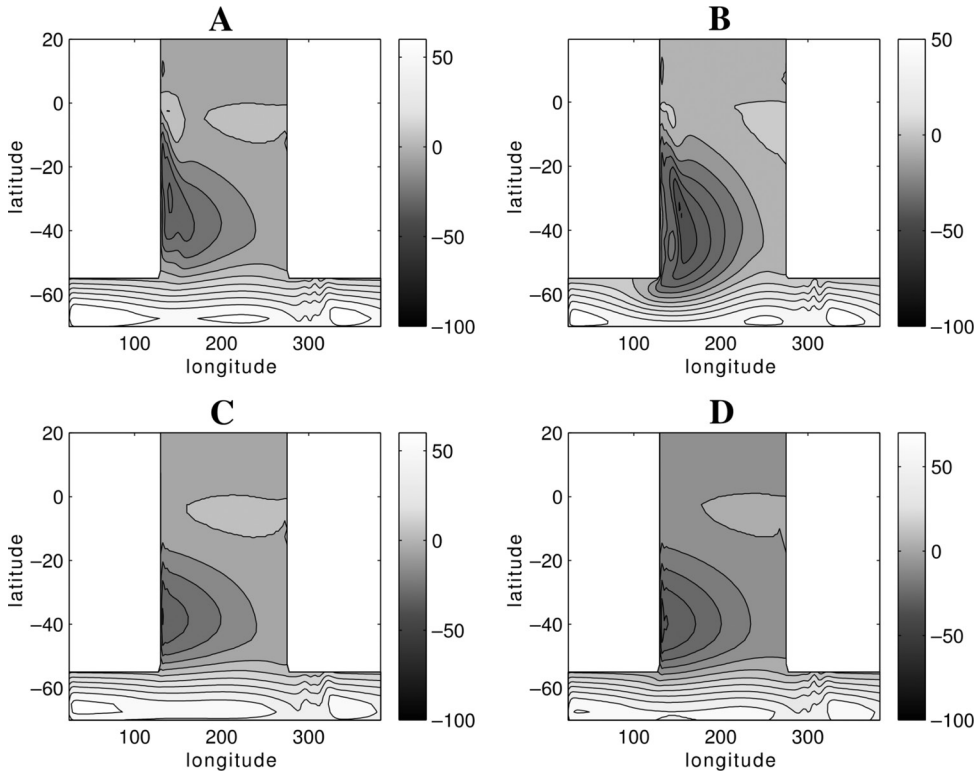

Figure 12. Stream function for the equilibrium solution, after 2000 years of integration. (a) Exp.STANDARD, (b) Exp.HIGH-RES, (c) Exp.NO-SHELF, and (d) Exp.FLAT. The units are in sverdrups.

and μ_S were retained to keep the same values in that experiment, in spite of the resolution being three times higher in the meridional direction. This led to effective increasing of the mixing, especially in the western boundary layer, (compared to the Exp.STANDARD) and a decrease in the amplitude of the anomaly by about 30%. We do not expect a decrease of this anomaly amplitude if these coefficients are corrected in a manner consistent with the increase in spatial resolution.

3.3. Experiment NO-SHELF (No Shelf in Western Pacific)

[48] The ACC transport decreases profoundly by about 25% to the value of 41.4 Sv (see Figure 12). The Pacific gyre has a simpler form compared to the experiments with a continental shelf (Exp.STANDARD and Exp.HIGH-RES), and is less stretched along the western boundary. The maximum value of the gyre transport is close to the Exp.STANDARD (i.e., −40.8 Sv).

[49] Interestingly, the temperature anomaly, propagated along the equator is of opposite sign (negative) compared to the experiments with a western shelf (Exp.STANDARD and Exp.HIGH-RES). The absolute amplitude of the anomaly decreases by factor of 2.5 compared to Exp.STANDARD. The signal also propagates more slowly, arriving at the eastern subdomain Eq4 45 days later than in Exp.STANDARD.

3.4. Experiment FLAT (Constant Depth in Pacific)

[50] The stream function looks similar to Exp.NO-SHELF. However, the ACC transport is much higher: 56.5 Sv. versus 41.4 Sv. in Exp.NO-SHELF (see Figure 12). In fact this is the highest ACC transport of all the experiments.

[51] The value of the propagating temperature anomaly along the equator has the same negative sign as Exp.NO-SHELF, and the opposite sign to experiments Exp.STANDARD and Exp.HIGH-RES with a "shelf" (Figure 10). The amplitude of the anomaly increased by factor of 2 compared to Exp.NO-SHELF, and reaches the value of -0.1° in the eastern equatorial subdomain Eq4. The signal propagates quicker than in the Exp.NO-SHELF but slower than in Exp.STANDARD.

3.5. Experiment STANDARD-E (SSS Anomaly East of Ridge)

[52] This experiment is based on the output of the equilibrium solution for the Exp.STANDARD, but the SSS disturbance was placed on the eastern side of the ACC bump. Other parameters of the disturbance are the same.

[53] The propagation of the temperature anomaly is similar to Exp.STANDARD, however with an opposite sign of anomaly: Figures 8 and 11 are highly anticorrelated. The amplitude increases (in absolute value) along the equator from west to east from -0.06°C at Eq2 after 90 days to -0.08 at Eq3 after 120 days, and to -0.14 at Eq4 after 180 days (compare these values with results of the section 3.1).

3.6. Experiment STANDARD-ONE (Anomaly 1 psu)

[54] This experiment was the same as Exp.STANDARD, but the initial SSS anomaly had half of the value of Exp.STANDARD and was applied for twice as long

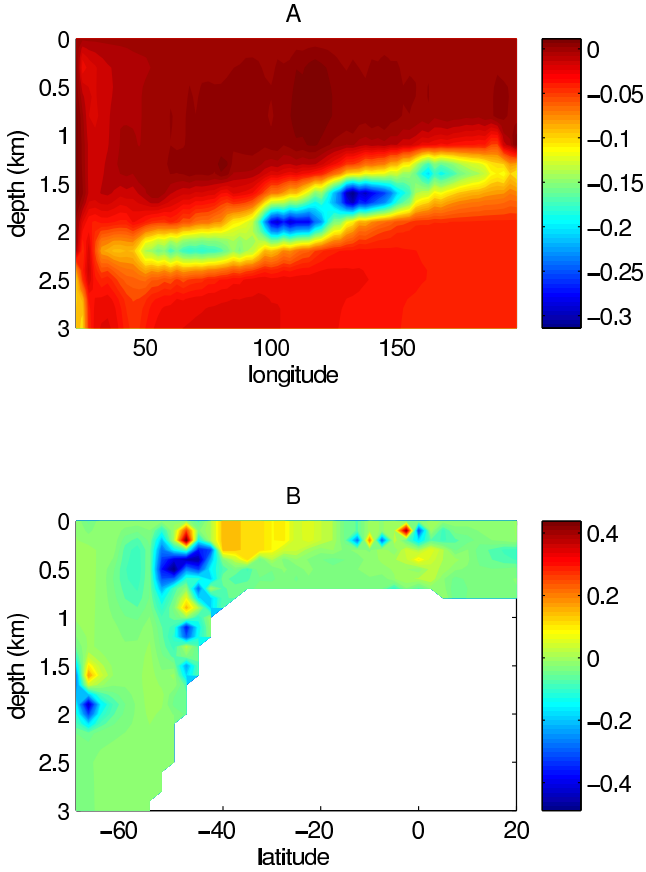

Figure 13. (a) The temperature anomaly along a zonal section at 70°S in Exp.STANDARD-QUARTER after 2 years. (b) The temperature anomaly along a meridional section at 127°E in Exp.STANDARD-QUARTER after 2 years. The units are in °C.

(120 days). The values of the temperature anomaly at the western equatorial subdomains are smaller than in the Exp.STANDARD by one third, but are more similar for the more eastern subdomains. In the easternmost subdomain Eq4, the maximum amplitude of 0.11 C° is almost the same as in Exp.STANDARD.

3.7. Experiment STANDARD-HALF (Anomaly 0.5 psu)

[55] This experiment was the same as Exp.STANDARD, but the initial SSS anomaly had a quarter of the value in the Exp.STANDARD and was set for four times longer (240 days).

[56] In previous subsections (3.1–3.6) the propagation of the signal has been studied paying the most attention to the direction and speed of propagation. For that purpose we integrated anomalies over 10° × 10° areas in the second layer in the model. However, the strongest signal does not necessarily occur in these arbitrarily defined areas. Furthermore, in some regions the largest amplitude anomalies can occur in the 3rd or 4th level. In some regions there is a dipole-like horizontal distribution in temperature anomaly, which results in a substantial reduction of the averaged value compared to the local maximum value in a particular model level.

[57] In this experiment we try to observe the highest values of anomaly in specific domains, like southwest Pacific, equatorial Pacific and around the Antarctic coast after two years of integration of the "anomaly" stage.

[58] The temperature anomaly near the Antarctic coast, far away of the source (between 30°E and 170°W) reaches −0.36°C and 0.27°C, as a result of Kelvin wave propagation.

[59] The strongest negative temperature anomaly develops in the southwestern Pacific, near the coast, and reaches −1.01°C at depth of 300–700 m, with a positive anomaly of 0.77°C in the upper 200 m. Near the western coast of the equatorial Pacific the anomaly demonstrates a persistent concentrated dipole-type distribution from about −0.59° to +0.57°C in the upper 150 m.

[60] In a zonal, along-equator section at 2.5°S, we observed that the temperature anomalies are concentrated in the upper 300 m near the western boundary, and reach values between −0.38° and +0.50°C. Further to the east, the strongest negative anomaly occurs at depth of 300–400 m, reaching −0.12°C and positive anomaly occurs near the eastern coast, reaching 0.09°C at depth of about 1 km. The distribution of the anomaly along the central and eastern equator is similar to that at the 2.5°S, reaching values between −0.14° and 0.08°C.

3.8. Experiment STANDARD-QUARTER (Anomaly 0.25 psu)

[61] This experiment was the same as Exp.STANDARD, but the initial SSS anomaly was set almost an order of magnitude smaller (0.25 psu) and for a duration of one year. Similar to the previous experiment (STANDARD-HALF) we try to observe the highest values of anomaly in the specific domains, like the southern west Pacific, equatorial Pacific and around the Antarctic coast after two years of integration of the anomaly stage.

[62] The highest resulting temperature anomaly in the ACC area is about +1.4°C at 260°E in the Bellingshausen Sea close to the coast. In the area between 220° and 300°E there exists a strong dipole of −2.5° to +2.0°C in the intermediate water. Convection processes in that area play an extraordinary role in the formation of such a distribution. The negative temperature anomaly near the Antarctic coast reaches −0.35°C, between 100° and 150°E, as a result of Kelvin wave propagation (Figure 13a).

[63] The strongest negative temperature anomaly develops in the southwest Pacific, near the coast, at depth of 300–700 m, and reaches −0.56°C (see Figure 13b), and the positive anomaly of 0.51°C in the upper 200 m. Near the western coast of the equatorial Pacific the anomaly demonstrates a persistent concentrated horizontal dipole-type distribution from about −0.40° to +0.53°C in the upper 150 m (see Figure 13b).

[64] In a zonal, along-equator section at 2.5°S, one can see that the temperature anomalies are concentrated in the upper 300 m near the western boundary, and reach values of −0.25° to +0.53°C (Figure 14a). Further to the east, the strongest negative anomaly occurs at the depths of 300–400 m, reaching −0.11°C. The positive anomaly near the eastern coast reaches 0.09°C at depth of about 1 km (Figure 14b). The dipole distribution of the temperature anomaly along the equatorial western Pacific can be clearly

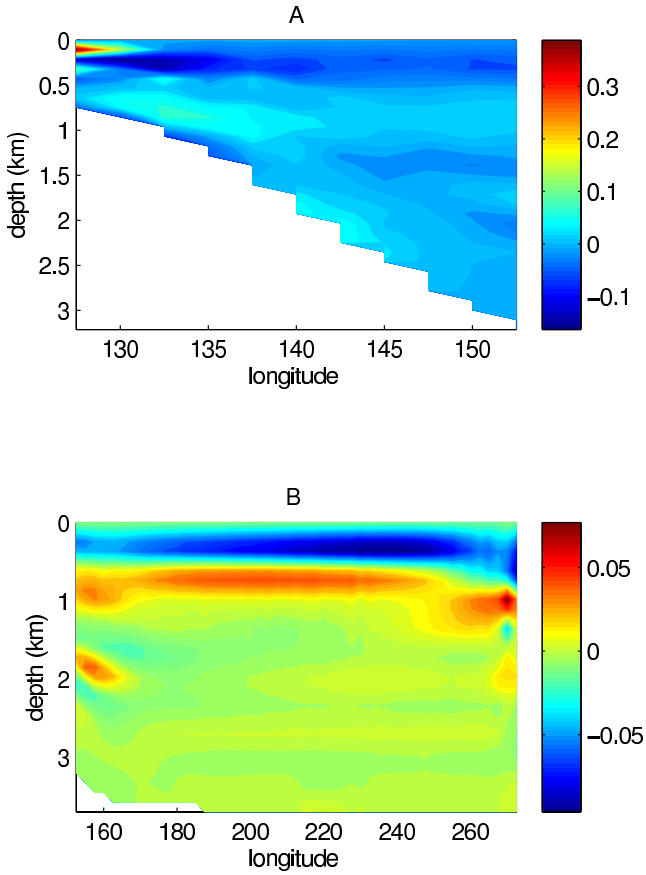

Figure 14. The temperature anomaly along a zonal section at 2.5°S in Exp.STANDARD-QUARTER after 2 years. The units are in °C.

seen on Figures 14a and 15a. The distribution of the anomaly along the central and eastern equator is similar to that in a section at 2.5°S and in the Exp.STANDARD-HALF, reaching values between −0.13° and 0.08°C (Figure 15b).

3.9. Experiment RIDGE (Ridge)

[65] This experiment was the same as Exp.STANDARD, but a new element of topography is introduced in the form of a large-scale ridge in the eastern part of the Pacific. The initial SSS anomaly was set to 2 psu for a period of 60 days. As quickly as in the Exp.STANDARD the anomaly reaches the western Pacific within days. At the beginning the amplitude is rather small but then increases greatly over time. The main difference with the previous experiments is that strong anomalies appear along the ridge. In the first 3–4 month the negative anomaly stretched along the eastern side of the ridge and the positive anomaly stretched along the western side (see Figure 16). After 200 days the anomaly along the ridge reaches the eastern equatorial Pacific. So, the eastern equatorial Pacific is influenced not only by Kelvin equatorial waves, but also by the anomaly, propagating along the ridge.

[66] In the southwestern Pacific, near the edge of the continental shelf, a large positive anomaly (up to 1.34°C after 2 years) forms near the 132.5°E section, down to 1.2 km depth (see Figure 17). This anomaly is stretched along the bottom topography (at depth of 1 km) and reaches the equator. At the equator, after 2 years the highest anomaly values occur near the surface (down to 150 m) near the western boundary and also at the depth of 1–1.5 km at the longitudes of 132.5°–140°E (values reaches 0.29° and −0.26°C).

4. Discussion and Conclusions

[67] In a number of recent studies, the global links between tropical ocean and Antarctic sea ice extent and other parameters have been revealed [*White and Peterson*, 1996; *Yuan et al.*, 1996; *Yuan and Martinson*, 2000; *Venegas and Drinkwater*, 2001; *Kwok and Comiso*, 2002]. Usually it is supposed that the signal originates in the tropics and propagates to the high latitudes in the Southern Hemisphere, rather than vice versa. In these previous studies there are either few explanations of the physical mechanisms responsible for such a link, or it is proposed that it takes place via the atmosphere. Generally speaking, such kinds of phenomena are a result of a coupled atmosphere-ocean-cryosphere system. If the characteristic timescale of this process is around one year or more, the ocean could be play an active progenitive role, rather then a passive dynamical/thermodynamical role. Our aim is to find a possible mechanism responsible for a link between the Antarctic and the tropical/equatorial ocean via the ocean.

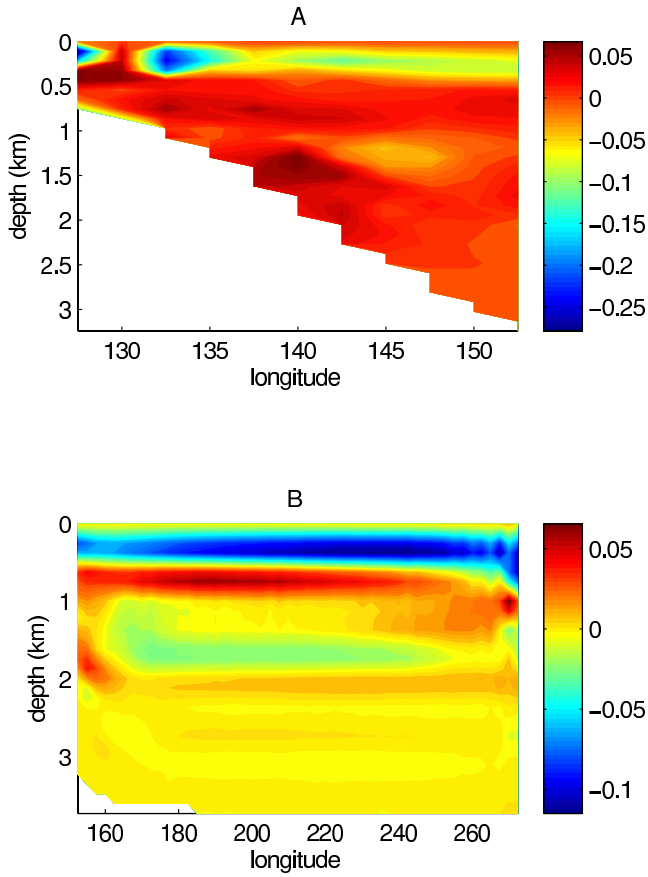

Figure 15. The temperature anomaly along a zonal section at the equator in Exp.STANDARD-QUARTER after 2 years. The units are in °C.

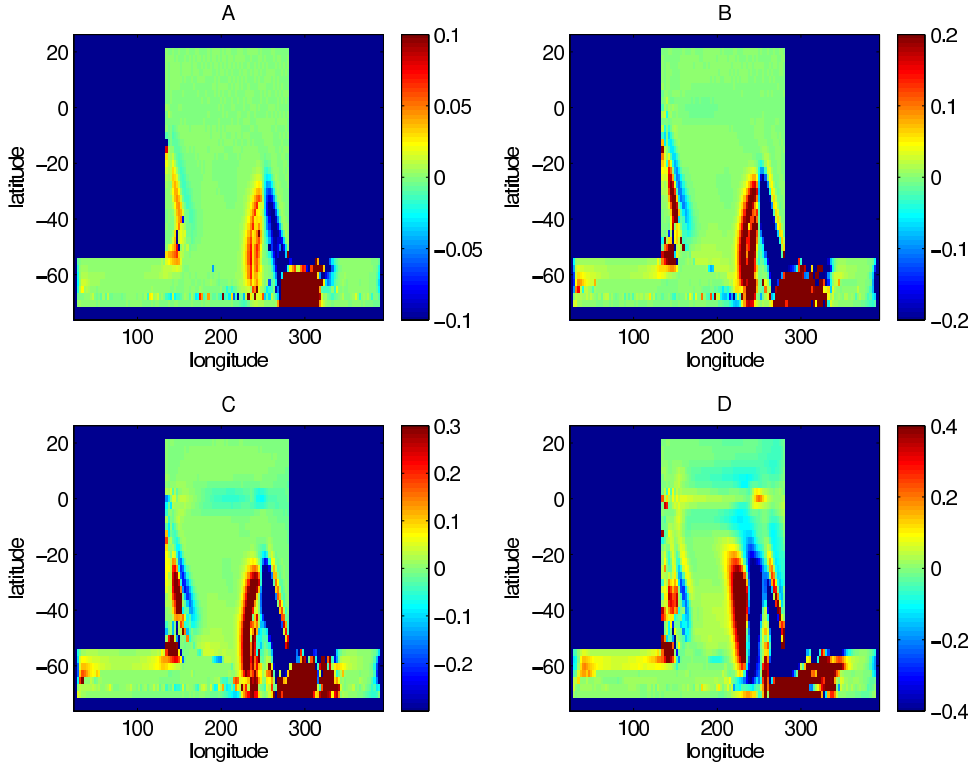

Figure 16. The subsurface temperature anomaly (at the second layer) at four consecutive times (t = (a) 30, (b) 60, (c) 120, and (d) 390 days) in Exp.RIDGE. The units are in °C.

[68] Advective processes in the ocean are rather slow, with timescales of hundreds of years. If the ocean is to play an active role in establishing a connection between the tropical ocean and the Antarctic, some other much quicker process must be invoked. One of the possible mechanisms is propagating waves, transporting signals very quickly across global ocean basins.

[69] It is well known that the coastal trapped Kelvin waves propagate along an ocean boundary anticlockwise (clockwise) in the Northern (Southern) Hemisphere [*Kawase*, 1987; *Johnson and Marshall*, 2002]. If the signal arrives at the equator on the western coast it propagates along the equator as an equatorial Kelvin wave. This scheme is evident for closed basins in the Northern Hemisphere. However, in the Southern Ocean there is a periodic quasi-zonal channel, where this scheme is not valid. So, the question is whether it is possible for a signal to propagate from a location in the Southern Ocean to the equatorial ocean, and particular to the eastern equatorial Pacific.

[70] Our results demonstrate that this depends on the opportunity for propagation of the signal in the ACC Belt, i.e., in the zonal channel existing at Drake Passage latitudes. Indeed, there is an effective and rapid response in the tropical ocean to anomalies initiated in the Southern Ocean. To understand the mechanism, a number of numerical experiments were carried out for a simple geometry ocean basin with a σ coordinate primitive equation model INM. Experiments have allowed us to find a potential missing link in the chain of anomaly transfer: we represent the whole scheme as follows (see Figure 18). 1. (The missed link)

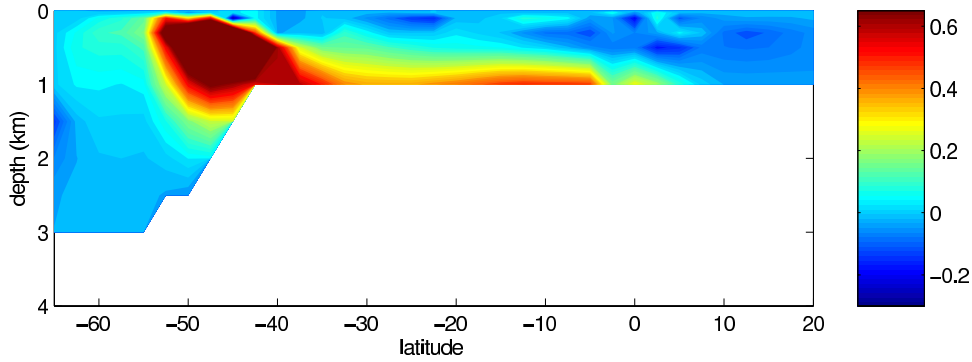

Figure 17. The temperature anomaly along a meridional section at 132.5°E in Exp.RIDGE after 2 years. The units are in °C.

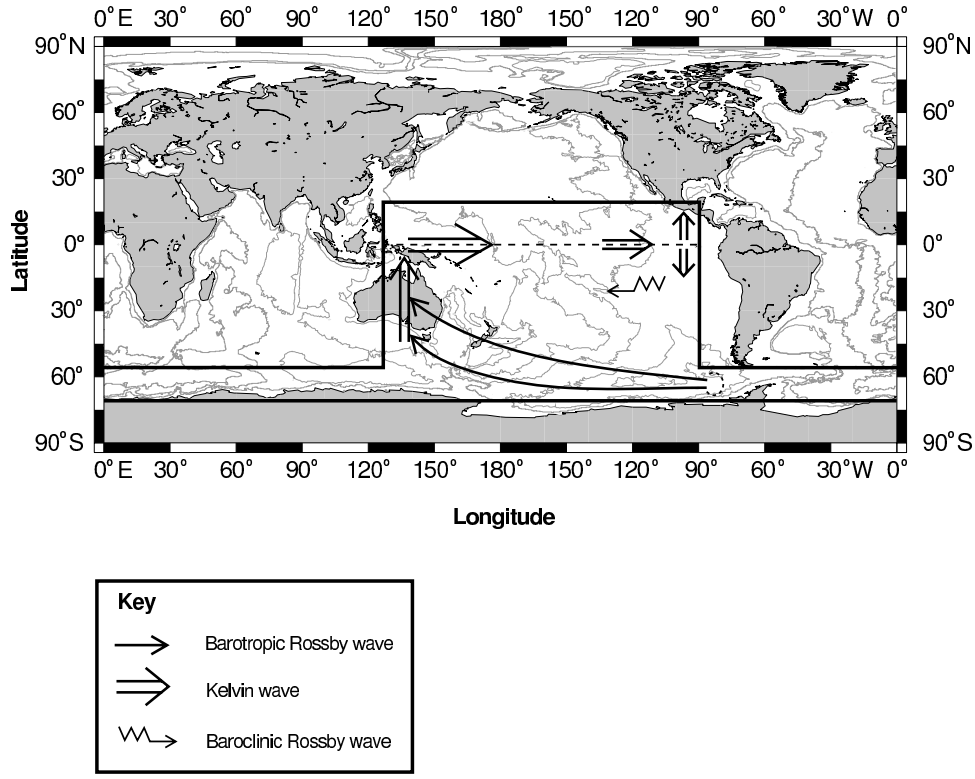

Figure 18. The scheme of the propagation of the signal from the Antarctic to the western, equatorial, and eastern Pacific. The solid arrow represents the barotropic Rossby wave, the double solid arrow represents the Kelvin wave, and the zig-zag arrow represents the baroclinic Rossby wave. The time of propagation of the barotropic Rossby wave from source area to the western Pacific and formation of the nonstationary boundary layer is 1–10 days. The time of the formation of the temperature anomaly along the western coast is around 30–50 days. The time of arrival of the maximum of the signal to the western (Eq2), middle (Eq3), and eastern (Eq4) subdomain is about 90, 120, and 180 days, respectively.

density anomalies, caused by sea ice-induced salinity anomalies above the variable bottom topography around Antarctica generate barotropic Rossby waves that quickly propagate to the western Pacific. 2. Interaction between the barotropic Rossby wave and a western ocean basin coastline generates a Kelvin wave-like boundary mode. 3. Because of this process, a density/temperature anomaly appears along the western Pacific boundary and moves equatorward. 4. This temperature anomaly propagates eastward along the equator to the eastern Pacific coast as a trapped equatorial Kelvin wave. 5. When the anomaly reaches the eastern coast, it generates poleward coastal Kelvin waves.

[71] As a consequence of the above chain of events, positive/negative temperature anomalies are formed near the eastern coast of the tropical Pacific. These events may reinforce or suppress ENSO cycles. In our experiments the formation of positive/negative temperature anomalies depends on several factors, such as initial position of the SSS anomaly relative to a topographic obstacle and bottom topography configuration in the western Pacific, i.e., existence of the western continental shelf. At the western continental shelf there is an acceleration in anomaly formation along the western coast. The anomaly generated at the equator near the western coast has the opposite sign to the anomaly in the experiment without a continental shelf. The western shelf excites a positive temperature anomaly, which itself contributes to acceleration of its propagation along the equator. The zonally averaged depth in the Pacific shows a south-north slope. This slope appears to be an obstacle to the signal developing: the absolute values of the signal decreases 2.5 times compared to the Exp.STANDARD, and is half the size of the Pacific flat bottom Exp.FLAT.

[72] The interaction of the barotropic Rossby waves with the bottom relief generates baroclinic modes. We found a quick response in the new introduced ridge (RIDGE experiment), simulating the East Pacific Rise. This ridge does not prevent the signal reaching the western Pacific. Similar to the basic experiment the amplitude at the beginning is rather small but greatly increases over time. For example the highest anomaly appears in the southern western Pacific and after two years it is 1.34°C. This anomaly "sits" at the edge of steep meridional slope and stretches from the surface down to 1.2 km. Toward the north the highest values along 132.5°E takes place near the bottom relief (about 1 km) and reaches the equator.

[73] The main difference with the previous experiments is that strong anomalies appear along the ridge. In the first 3–4 months a negative (positive) anomaly is stretches along the eastern (western) side of the ridge. After 200 days the anomaly along the ridge reaches the eastern equatorial Pacific. So, the eastern equatorial Pacific is influenced not

only by equatorial Kelvin waves, but also by the anomaly propagating along the ridge.

[74] Overall, the amplitude of SST anomaly response is stronger if (1) the duration of the initial disturbance is longer (note that in our experiments a decrease in the value of initial salinity anomaly does not lead to a decrease in temperature response on the equator, provided that the initial disturbance has a longer duration) and (2) the ACC transport is higher (note that the ACC transport in our experiments is at least three times smaller than it is in reality because of the simplified domain/topography configuration).

[75] We suggest that use of a smaller restoring coefficient or ''flux boundary conditions'' (instead of ''restoring boundary conditions'') also enhance the amplitude of response; however these hypotheses are speculative and need to be checked. External parameters, such as topography and model space resolution would also affect the equatorial response.

[76] The important question is: where does the energy of the initiating process come from and where is it transferred? Introducing a salinity anomaly changes the potential energy and potential energy is exchanged for kinetic energy. For the closed basin the pressure work term is equal to the buoyancy term [*Treguier*, 1992; *Ivchenko et al.*, 1997]. The pressure work term can be split between external (depth averaged) and internal (the remaining) parts. In the presence of topography and a density gradient the JEBAR term (Joint Effect of Baroclinicity and Relief) [*Sarkisyan*, 1977] provides an exchange between internal and external parts of the pressure gradient work (their sum is zero) (see Appendix B). So, the buoyancy term allows an exchange between potential and kinetic energy. The JEBAR term thus enables redistribution between internal and external modes of the kinetic energy [*Ivchenko et al.*, 1997]. Barotropic Rossby waves (external mode) propagate mainly westward to interact with the western Pacific boundary and to produce internal (baroclinic) signals.

[77] Our main efforts have been applied to studying the mechanisms of the rapid response of the western and equatorial Pacific to an initial anomaly first generated at a specific, distant position in the Antarctic Circumpolar Current area (like Drake Passage or Weddell Sea). It was shown that switching off the barotropic Rossby waves prevents generation of the western boundary modes and, as a result, the temperature field remains undisturbed. The amplitude of the disturbed temperature field in the western Pacific is not small. Even in the experiment with the smallest initial disturbance (0.25 psu) the local temperature anomalies reached -0.56° and $+0.51^\circ$C in the southwest Pacific, with values in the western equatorial Pacific between -0.40° and $+0.53^\circ$C. Note that the greatest positive and negative anomalies along equator in the central and eastern Pacific usually happen after 3–7 months, i.e., earlier than after 2 years (the time corresponding to the Figures 13–15).

[78] Importantly, the initial disturbance has to happen in the vicinity of steep topography, because the main source of the generated barotropic Rossby waves depend on the Joint Effect of Baroclinicity and Relief. The JEBAR effect deviates from zero only if there are horizontal density gradients together with sloping bottom relief. The steeper the topography, the bigger the source of barotropic Rossby waves (see Appendix B). Note that deep convection above steep topography also enhances the generation of barotropic Rossby waves.

[79] The fastest moving signal along the equatorial Pacific is propagated by the means of the first mode of the equatorial trapped wave. The sign of incoming temperature anomalies to the eastern part of equatorial basin depends on the disturbed temperature field in the western part of equatorial Pacific, as well as on the equilibrium regime. The structure of the actual disturbed temperature field in the western equatorial Pacific is dependent on the incoming barotropic signal and on the generated baroclinic response.

[80] We acknowledge that, because the horizontal resolution in the model is not high enough for equatorial dynamics, the analytical estimates of the equatorial Kelvin wave propagation can deviate from the numerical solution.

[81] It is difficult to say whether natural variability in the Southern Ocean creates an initial perturbation/anomaly strong enough to influence the coupled atmosphere-ocean system in the equatorial Pacific, or indeed whether barotropic Rossby waves are a common phenomenon as a consequence of typical interannual variations in sea ice conditions, and/or other changes in the coupled atmosphere-ice-ocean system, such as freshwater anomalies initiated by the Larsen ice shelf collapse, or Heinrich-like events. The latter theme shall be a focus for future study.

[82] The proposed mechanism allows us to estimate the time of equatorial response to major rapid changes in the high latitudes. This mechanism could, under the right circumstances, have significance with respect to rapid extratropical tropical oceanic links. Furthermore it may provide a missing link with respect to two-way interactions and teleconnections between Antarctic sea ice conditions and El Nino–Southern Oscillation.

Appendix A: INM Model

[83] The wind stress was derived from 1990–1995 time averaged ECMWF wind, by taking zonal average over the Pacific. Then a polynomial approximation to that field was used:

$$A(y) = p(1)*y^5 + p(2)*y^4 + p(3)*y^3 + p(4)*y^2 + p(5)y + p(6), \quad \text{(A1)}$$

where $p(1) = 72.9191$; $p(2) = 22.2569$; $p(3) = -28.0610$; $p(4) = -4.6605$; $p(5) = 0.3888$; $p(6) = -0.2599$; and y is a latitude normalized by factor of 100. Also, a similar fifth order polynomial approximations were developed for the zonally averaged surface temperature and salinity over the Pacific from the *Levitus* [1982] climatology, (see Figure 2), with coefficients: $p_{temp}(1) = -103.3461$; $p_{temp}(2) = 7.6653$; $p_{temp}(3) = 36.6439$; $p_{temp}(4) = -70.6298$; $p_{temp}(5) = 2.1528$; $p_{temp}(6) = 28.3550$; $p_{sal}(1) = 0.1915$; $p_{sal}(2) = 0.3099$; $p_{sal}(3) = 0.1387$; $p_{sal}(4) = -0.0023$; $p_{sal}(5) = -0.0080$; $p_{sal}(6) = 0.0347$; In the paper the temperature and salinity are in °C and in psu, respectively.

[84] This model was developed in the Institute of Numerical Mathematics, Moscow [*Zalesny*, 1996]. The model is based on the primitive equation system of thermohaline ocean dynamics. The governing equations are written

in the bottom following system of coordinates (σ system); as a result the bottom relief is a smooth function of the horizontal coordinates (not step function, as in the z coordinate). That allows a better description of the dynamical processes of interaction between waves and currents with bottom topography. This is important for the studies where such interaction is important.

[85] The numerical algorithm of the model is based on the implicit splitting scheme. The space approximation of the model equations is realized on C grid.

[86] The model equations in the spherical coordinates λ, θ, z are

$$\frac{du}{dt} - (l - m\cos\theta u)v = -\frac{m}{\rho_0}\frac{\partial p}{\partial \lambda} + \frac{\partial}{\partial z}\nu_u\frac{\partial u}{\partial z} + F^u, \tag{A2}$$

$$\frac{dv}{dt} + (l - m\cos\theta u)u = -\frac{n}{\rho_0}\frac{\partial p}{\partial \theta} + \frac{\partial}{\partial z}\nu_v\frac{\partial v}{\partial z} + F^v, \tag{A3}$$

$$\frac{\partial p}{\partial z} = g\rho, \tag{A4}$$

$$m\left[\frac{\partial u}{\partial \lambda} + n\frac{\partial}{\partial \theta}\left(\frac{v}{m}\right)\right] + \frac{\partial w}{\partial z} = 0, \tag{A5}$$

$$\frac{dT}{dt} = \frac{\partial}{\partial z}\nu_T\frac{\partial T}{\partial z} + F^T, \tag{A6}$$

$$\frac{dS}{dt} = \frac{\partial}{\partial z}\nu_S\frac{\partial S}{\partial z} + F^S, \tag{A7}$$

$$\rho = f(T, S, p), \tag{A8}$$

$$\begin{aligned} \frac{d}{dt} &= \frac{\partial}{\partial t} + mu\frac{\partial}{\partial \lambda} + nv\frac{\partial}{\partial \theta} + w\frac{\partial}{\partial z}, \\ F* &= m^2\frac{\partial}{\partial \lambda}\mu_*\frac{\partial *}{\partial \lambda} + mn\frac{\partial}{\partial \theta}\mu_*\frac{n}{m}\frac{\partial *}{\partial \theta}. \end{aligned} \tag{A9}$$

[87] Here, λ is the longitude, $\theta = 90° + \phi$, ϕ is the latitude, z is the vertical downward coordinate, (u, v, w) is the velocity field, T is potential temperature, S is salinity, p is pressure, ρ is density given by the UNESCO-80 formula; ν_u, ν_v, ν_T, ν_S are the coefficients of vertical turbulent diffusivity; μ_u, μ_v, μ_T, μ_S are the corresponding coefficients of horizontal diffusivity; l is the Coriolis parameter: $l = -2\Omega\cos\theta$; $m = \frac{1}{R\sin\theta}$, $n = \frac{1}{R}$, R is the radius of the earth.

[88] To parameterize deep vertical convection the turbulent coefficients ν_T, ν_S are chosen as nonlinear functions depending on density gradient [*Schmidt and Mysak*, 1996]:

$$\nu_T = \nu_S \equiv \nu_{\min}\exp\left\{a\left[1 - th\left(\gamma\frac{\partial \rho}{\partial z}\right)\right]\right\},$$

where $\nu_{\min}$, γ are positive constants and $a = \frac{1}{2}\ln\left\{\frac{n_{\max}}{n_{\min}}\right\}$.

[89] The system of equations (A2)–(A8) in the time interval (0, t] is considered in the three-dimensional domain D. D is bounded by the piecewise lateral boundary ∂D that is composed of the sea surface $z = 0$, the lateral surface Σ, and the bottom relief $H(\lambda, \theta)$. These equations are supplemented by corresponding boundary conditions.

[90] At the sea surface are used:

$$\nu_u\frac{\partial u}{\partial z} = -\frac{\tau_\lambda}{\rho_0}, \qquad \nu_v\frac{\partial v}{\partial z} = -\frac{\tau_\theta}{\rho_0}, \qquad w = 0, \tag{A10}$$

$$\nu_T\frac{\partial T}{\partial z} = \alpha\left(T - SST_{eq}\right), \qquad \nu_S\frac{\partial S}{\partial z} = \alpha\left(S - SSS_{eq}\right), \tag{A11}$$

where SST_{eq} and SSS_{eq} are the equilibrium values of the temperature and salinity. For the anomaly experiments we added the prescribed value of anomaly of sea surface salinity (ASSS) to the SSS_{eq} in A11, i.e.:

$$\nu_S\frac{\partial S}{\partial z} = \alpha\left(S - \left(SSS_{eq} + ASSS\right)\right). \tag{A12}$$

where ASSS = prescribed value of anomaly if $t < T_0$ and ASSS = 0, if $t \geq T_0$. For example, ASSS = 2 psu and T_0 = 60 days for the experiment STANDARD.

[91] The choice of the approximation and numerical solution of the system (A2)–(A8) is made under some transformations and involves a number of successive steps [*Zalesny*, 1996]:

[92] 1. The initial system (A2)–(A8) is rewritten in the σ coordinate (λ, θ, σ), where $\sigma = z/H(\lambda, \theta)$.

[93] 2. The system of equations is transformed to evolutionary form. For this purpose, the pressure p and the vertical velocity w are eliminated by representing the velocity vector components u, v as $u = \overline{u} + u'$, $v = \overline{v} + v'$ and introducing the stream function Φ for vertical-averaged flow;

[94] 3. The obtained system of evolutionary equations for the stream function Φ, deviations of the horizontal velocities u', v' from its vertical mean, temperature T and salinity S are written in symmetrized form. The form is chosen so that it is convenient to represent the operator of the differential problem as a sum of more simple suboperators. Each suboperator is nonnegative.

[95] 4. In order to solve the transformed problem the weak approximation method is employed. The differential problem is split into a chain of simpler evolutionary systems, and each of them is then approximated with respect to geometric coordinates (C grid) and time.

[96] There are two key features of the ocean numerical model used: symmetrized representation of equations in σ coordinates and the numerical algorithm based on splitting by physical processes and geometrical coordinates. The advantage of this transformed coordinate system from computational point of view is evident: there is no longer the problem of having a vertical coordinate level intersect the ocean bottom because the $\sigma = 1$ level follows the model's topography precisely. It permits a natural treatment of the bottom boundary layer, an accurate implementation of the bottom boundary conditions, and a simple numerical description of the model arrays with respect to the vertical. However, numerical σ models have difficulty in representing the horizontal pressure gradient (HPG) because of its

more complicated structure [*Griffies et al.*, 2000]. Usually, this leads to two undesirable consequences: a significant truncation error in the HPG terms and the deterioration of the computational stability of models. In our model the HPG representation is governed by the semidivergent form of the heat/salt transport operator and this form is symmetrized. It leads to a finite difference scheme which has two important properties [*Marchuk et al.*, 2003]: (1) valid discrete law of conservation of total energy and (2) no truncation error in the case of the horizontally uniform, linearly depth-stratified ocean with an arbitrary bottom relief.

Appendix B: Energy Conversion

[97] The kinetic energy equation, integrated over a fixed volume V can be written in the following form [*Holland*, 1975]:

$$\frac{\partial E}{\partial t} = A + G + B + W + D \tag{B1}$$

where E represents kinetic energy integrated over a fixed volume; A and G are the advection of kinetic energy into the region across the boundary and work by pressure forces at the boundary as a consequence of flow across the boundary, respectively; B is work done by buoyancy forces in the interior of the fluid; W and D are the work by surface wind stress and dissipation, respectively.

[98] For the closed basin (where the normal components of velocity on the boundary are zero) this equation is simplifying:

$$\frac{\partial E}{\partial t} = B + W + D \tag{B2}$$

[99] The buoyancy term is:

$$B = -\int_{(V)} w\,\rho g\,dV. \tag{B3}$$

[100] Separating kinetic energy into the external (depth averaged velocity) mode and internal (the rest) one can see that buoyancy term provides energy transfer between potential energy and internal mode of kinetic energy. In the following, index i refers to the internal mode, and e refers to the external mode. Another term, T, relating to the JEBAR effect (Joint Effect of Baroclinicity and Relief) appears in the presence of variable topography and a variable density field. This term exchanges between internal and external modes [*Treguier*, 1992; *Ivchenko et al.*, 1997]:

$$T = -\int_{(S)} \left(p^e - p^b\right) u_m^e \frac{\partial H}{\partial x_m}\,dS$$

where H is the ocean depth and S is the horizontal surface of the domain; p^b is the bottom pressure; here summation is implied over index m = 1, 2, representing horizontal coordinates (m = 1 and m = 2 are zonal and meridional coordinates, respectively).

[101] One can see that energy equations for the external and internal modes comprise pressure work terms, PW_e and PE_i [*Treguier*, 1992]:

$$\begin{aligned} PW_e &= -\int_{(V)} u_m^e \frac{\partial p}{\partial x_m} dV \\ PW_i &= -\int_{(V)} u_m^i \frac{\partial p}{\partial x_m} dV \end{aligned} \tag{B4}$$

[102] So, we can write for the closed basin that

$$\begin{aligned} PW_e &= T \\ PW_i &= B - T. \end{aligned} \tag{B5}$$

[103] The transfer from/to potential energy (B) appeared in the internal mode and by T term is redistributing between internal and external modes.

[104] **Acknowledgments.** P. Killworth suggested that the analysis of the mode propagation along the equator would reveal the changes of the sign of the anomaly. We had helpful conversations with S. Danilov. We are grateful to them. We thank D. Holmes for fruitful discussions. Comments offered by anonymous reviewers and J. Richman were very helpful in improving the presentation of this paper. V. O. Ivchenko was supported by a National Research Council Senior Resident Research Associateship while working at the Jet Propulsion Laboratory (U.S.A.), by the Alfred Wegener Institute of Polar and Marine Research (Germany), and by the National Environmental Research Council (U.K.) as part of the Rapid Climate Change (RAPID) Programme. V. B. Zalesny was supported by the Russian Foundation for Basic Research. M. R. Drinkwater performed part of this work in the Polar Oceanography Group at the Jet Propulsion Laboratory, California Institute of Technology, with the support of NASA Code Y, prior to moving and completing it with the European Space Agency, Science and Application Department.

References

Bromwich, D. H., B. Chen, and K. M. Hines (1998), Global atmospheric impacts induced by year-round open water adjacent to Antarctica, *J. Geophys. Res.*, *103*, 11,173–11,189.

Carleton, A. M. (1988), Sea ice-atmosphere signal of the Southern Oscillation in the Weddell sea, Antarctica, *J. Clim.*, *1*, 379–388.

Cunningham, S., S. Alderson, and B. King (2003), Transport and variability of the Antarctic Circumpolar Current in Drake Passage, *J. Geophys. Res.*, *108*(C5), 8084, doi:10.1029/2001JC001147.

Delecluse, P., and V. B. Zalesny (1996), Problems of numerical modelling of equatorial dynamics, *Oceanology*, *36*, 26–42.

Drinkwater, M. R., X. Liu, and S. Harms (2001), Combined satellite- and ULS-derived sea-ice flux in the Weddell Sea, Antarctica, *Ann. Glaciol.*, *33*, 125–132.

Grezio, A., N. C. Wells, V. O. Ivchenko, and B. A. deCuevas (2005), Dynamical budgets in the Antarctic Circumpolar Current using ocean general circulation models, *Q. J. R. Meteorol. Soc.*, *131*, 833–860.

Griffies, S. M., C. Böning, F. O. Bryan, E. P. Chassignet, R. Gerdes, H. Hasumi, A. Hirst, A.-M. Treguier, and D. Webb (2000), Developments in ocean climate modelling, *Ocean Modell.*, *2*, 123–192.

Harms, S., E. Fahrbach, and V. H. Strass (2001), Sea ice transport in the Weddell Sea, *J. Geophys. Res.*, *106*, 9057–9073.

Holland, W. R. (1975), Energetics of baroclinic oceans, in *Numerical Models of Ocean Circulation*, pp. 168–177, Natl. Acad. Press, Washington, D. C.

Ivchenko, V. O., K. J. Richards, and D. P. Stevens (1996), The dynamics of the Antarctic Circumpolar Current, *J. Phys. Oceanogr.*, *26*, 753–774.

Ivchenko, V. O., A. M. Treguier, and S. E. Best (1997), A kinetic energy budget and internal instabilities in the Fine Resolution Antarctic model, *J. Phys. Oceanogr.*, *27*, 5–22.

Ivchenko, V. O., V. B. Zalesny, and M. R. Drinkwater (2004), Can equatorial ocean quickly respond to Antarctic sea ice/salinity anomalies?, *Geophys. Res. Lett.*, *31*, L15310, doi:10.1029/2004GL020472.

James, I. N. (1988), On the forcing of planetary-scale Rossby waves by Antarctica, *Q. J. R. Meteorol. Soc.*, *114*, 619–637.

Johnson, H. L., and D. P. Marshall (2002), A theory for the surface Atlantic response to thermohaline variability, *J. Phys. Oceanogr.*, *32*, 1121–1132.

Karoly, D. J. (1989), Southern Hemisphere circulation features associated with El Nino–Southern Oscillation events, *J. Clim.*, *2*, 1239–1252.

Kawase, M. (1987), Establishment of deep ocean circulation driven by deep-water production, *J. Phys. Oceanogr.*, *17*, 2294–2317.

Kwok, R., and J. C. Comiso (2002), Southern Ocean climate and sea ice anomalies associated with the Southern Oscillation, *J. Clim.*, *15*, 487–501.

Levitus, S. (1982), Climatological atlas of the world oceans, *NOAA Prof. Pap. 13*, U.S. Gov. Print. Off., Washington, D. C.

Lighthill, M. J. (1969), Dynamic response of the Indian Ocean to onset of the southwest monsoon, *Philos. Trans. R. Soc., Ser. A*, *265*, 45–92.

Marchuk, G. I., J. Schröter, and V. B. Zalesny (2003), Numerical study of the global ocean equilibrium circulation, *Russ. J. Numer. Anal. Math. Modell.*, *18*, 307–335.

Meredith, M. P., P. L. Woodworth, C. W. Hughes, and V. Stepanov (2004), Changes in the ocean transport through Drake Passage during the 1980s and 1990s, forced by changes in the Southern Annular Mode, *Geophys. Res. Lett.*, *31*, L21305, doi:10.1029/2004GL021169.

Mo, K. C., and G. H. White (1985), Teleconnections in the Southern Hemisphere, *Mon. Weather Rev.*, *113*, 22–37.

Olbers, D., and V. O. Ivchenko (2001), On the meridional circulation and balance of momentum in the Southern Ocean of POP, *Ocean Dyn.*, *52*, 79–93.

Orsi, A. H., and T. Whitworth (2005), *Hydrographic Atlas of the World Ocean Circulation Experiment (WOCE)*, vol. 1, *Southern Ocean*, 223 pp., WOCE Int. Proj. Off., Univ. of Southampton, Southampton, U. K.

Peng, G. B., and P. K. Wang (1989), Influence of the Antarctic sea ice on the northwest Pacific sub-tropical high and its background of ocean-atmosphere circulation, *Chin. Sci. Bull.*, *34*, 1463–1465.

Peterson, R. G., and W. B. White (1998), Slow teleconnections linking the Antarctic Circumpolar Wave with the tropical El Nino–Southern Oscillation, *J. Geophys. Res.*, *103*, 24,573–24,583.

Philander, S. G. H., and R. C. Pacanovsky (1980), The generation of equatorial currents, *J. Geophys. Res.*, *85*, 1123–1136.

Richardson, G., M. R. Wadley, K. J. Heywood, D. P. Stevens, and H. T. Banks (2005), Short-term climate response to a freshwater pulse in the Southern Ocean, *Geophys. Res. Lett.*, *32*, L03702, doi:10.1029/2004GL021586.

Sarkisyan, A. S. (1977), *Numerical Analysis and the Prediction of Sea Currents*, 183 pp., Gidrometeoizdat, Saint Petersburg, Russia.

Schmidt, G. A., and L. A. Mysak (1996), The stability of a zonally averaged thermohaline circulation model, *Tellus, Ser. 1*, *48*, 158–178.

Simmonds, I., and T. H. Jacka (1995), Relationship between the interannual variability of Antarctic sea ice and the Southern Oscillation, *J. Clim.*, *8*, 637–647.

Stephens, C., J. I. Antonov, T. P. Boyer, M. E. Conkright, R. A. Locarnini, T. D. O'Brien, and H. E. Garcia (2002), *World Ocean Atlas, 2001*, vol. 1, *Temperature* [CD-ROM], *NOAA Atlas NESDIS*, vol. 49, edited by S. Levitus, 167 pp., U.S. Gov. Print. Off., Washington, D. C.

Strass, V. E., and E. Fahrbach (1998), Temporal and regional variation in sea ice drift and coverage in the Weddell Sea obtained from upward looking sonars, in *Antarctic Sea Ice: Physical Processes, Interactions and Variability*, *Antarct. Res. Ser.*, vol. 74, edited by M. O. Jeffries, pp. 123–139, AGU, Washington, D. C.

Timmermann, R. A., A. Beckmann, and H. H. Hellmer (2001), The role of sea ice in the fresh-water budget of the Weddell Sea, Antarctica, *Ann. Glaciol.*, *33*, 419–424.

Treguier, A. M. (1992), Kinetic energy analysis of an eddy resolving, primitive equation model of the North Atlantic, *J. Geophys. Res.*, *97*, 687–701.

Trenberth, K. E., G. W. Branstator, D. Karoly, A. Kumar, N.-C. Lau, and C. Ropelewski (1998), Progress during TOGA in understanding and modelling global teleconnections associated with tropical sea surface temperatures, *J. Geophys. Res.*, *103*, 14,291–14,324.

Turner, J. (2004), The El Nino–Southern Oscillation and Antarctica, *Int. J. Clim.*, *24*, 1–31.

Venegas, S., and M. R. Drinkwater (2001), Sea ice, atmosphere and upper ocean variability in the Weddell Sea, Antarctica, *J. Geophys. Res.*, *106*, 16,747–16,766.

Venegas, S., M. R. Drinkwater, and G. Schaffer (2001), Coupled oscillations in the Antarctic sea-ice and atmosphere in the South Pacific sector, *Geophys. Res. Lett.*, *28*, 3301–3304.

White, W. B., and R. G. Peterson (1996), An Antarctic circumpolar wave in surface pressure, wind, temperature and sea-ice extent, *Nature*, *380*, 699–702.

Yuan, X., and D. G. Martinson (2000), Antarctic sea ice extent variability and its global connectivity, *J. Clim.*, *13*, 1697–1717.

Yuan, X., M. A. Cane, and D. G. Martinson (1996), Cycling around the South Pole, *Nature*, *380*, 673–674.

Zalesny, V. B. (1996), Numerical simulation and analysis of the sensitivity of large-scale ocean dynamics, *Russ. J. Numer. Anal. Math. Modell.*, *11*, 421–443.

Zhang, Y., and A. J. Semtner (2001), The Antarctic Circumpolar Wave in a global, high-resolution coupled ice-ocean model, *Ann. Glaciol.*, *33*, 539–544.

M. R. Drinkwater, European Space Research and Technology Centre, European Space Agency, Keplerlaan 1, 2201AZ Noordwijk, Netherlands.

V. O. Ivchenko, National Oceanography Centre Southampton, European Way, Southampton SO14 3ZH, UK. (voi@noc.soton.ac.uk)

J. Schröter, Alfred Wegener Institute for Polar and Marine Research, Bussestrasse 24, D-27570 Bremerhaven, Germany.

V. B. Zalesny, Institute of Numerical Mathematics, Russian Academy of Sciences, Gubkin str. 8, 119991 Moscow, Russia.